In-plane elasticity of beetle elytra inspired sandwich cores

Xindi Yu [a],[*], Qicheng Zhang [a],[b], Athina Kontopoulou [a], Giuliano Allegri [a], Mark Schenk [a], Fabrizio Scarpa [a]

[a] Bristol Composites Institute, School of Civil, Aerospace and Mechanical Engineering (CAME), University of Bristol, University Walk, Bristol BS8 1TR, UK
[b] Faculty of Science and Engineering, Swansea University, Swansea SA1 8EN, UK

ARTICLE INFO

ABSTRACT

The Beetle Elytron Plate (BEP) is a new class of biomimetic sandwich core that features excellent compressive strength, energy absorption capacity and flexural properties. These characteristics make BEPs suitable as potential replacements of classical honeycomb cores in sandwich panels. This work describes the behaviour of the in-plane engineering elastic constants of parametric BEP topologies for the first time. The beetle elytron cores configurations are simulated using Finite Element models, including full-scale models and representative unit cells with periodic boundary conditions for asymptotic homogenization. The models are also benchmarked against experimental results obtained from ASTM tensile tests related to the in-plane Young's modulus, Poisson's ratio and shear modulus. The benchmarked models are then used to perform a parametric analysis against the geometry characteristics of the cellular configurations. Results obtained from this work will provide a solid foundation for further research on BEP structures and expand their applications into wider engineering fields.

1. Introduction

Sandwich structures are composed of thin skins and hollow core layers. Sandwich panels offer several advantages in terms of mechanical properties, such as light weight, high strength and specific stiffness [1–3]. Hence, sandwich panels are used in many engineering applications, ranging from aerospace [4,5], civil [6–8], marine [9,10] as well as in biomedical areas [11–13]. A wide variety of core types are used to meet design requirements, including foams [14–17], trusses [18–20] and cellular structures [21–23]. Bionics also have played a very important role in the development of new types of core materials. In nature, to survive and adapt to the natural environment, living beings tend to generate some unique biological structures with special functions as a result of their evolution history [24 25]. Thus, bio-inspired sandwich structures [26–28] have recently attracted significant research interest. Tasdemirci *et al* investigated a thin-walled structure inspired from the Balanus barnacle from both an experimental and a numerical standpoint, with emphasis on load-carrying and energy absorption applications [29]. Abo Sabah *et al* designed a novel sandwich beam inspired by the woodpecker's head, achieving an enhanced low-velocity impact behaviour [30]. It is well known that honeycomb (hexagonal) tessellations are often encountered in biological systems.4 The mechanical properties of honeycombs, such as compression

[31–33], high energy dissipation [34–36], impact resistance [37–40], and ballistic performance [41], are always of critical importance for a wide range of applications in aerospace [42], transportation [43–45] and civil engineering [46,47].

Beetles are present in our planet since the earliest Permian (295 million years ago) [48]. Beetles are characterized by the presence of an elytra that possess a remarkable three-dimensional structure to protect the body of the insect and also to facilitate its flight. The elytra features specific mechanical configurations [49], cuticles [50] and structural colors [50]. The beetle elytra are considered a class of high-strength, lightweight biological structures [51–53]. In 1994, Xiang *et al.* described the beetle elytron as a sandwich structure consisting of upper and lower skins, and a trabecular core structure [54]. Chen et al. reported that in the elytron of the *Allomyrina dichotoma* (*A. dichotoma*) beetle (Fig. 1a, red circle showing its forewings/elytra) thousands of trabeculae are present (Fig. 1b) [55]. A bionic-inspired sandwich plate based on the microstructure of the elytron of the *A. dichotoma* beetle [56,57], characterized by a hollow-trabecula honeycomb core structure, was proposed as early as 2003 [58]. The same configuration was then progressively modified during the following decade, and named as Beetle Elytron Plate in 2016 [59]. Observing the architecture of the *A. dichotoma* elytron shows that not all trabeculae are located at the intersections of the cell walls, as approximately 10% of trabeculae are
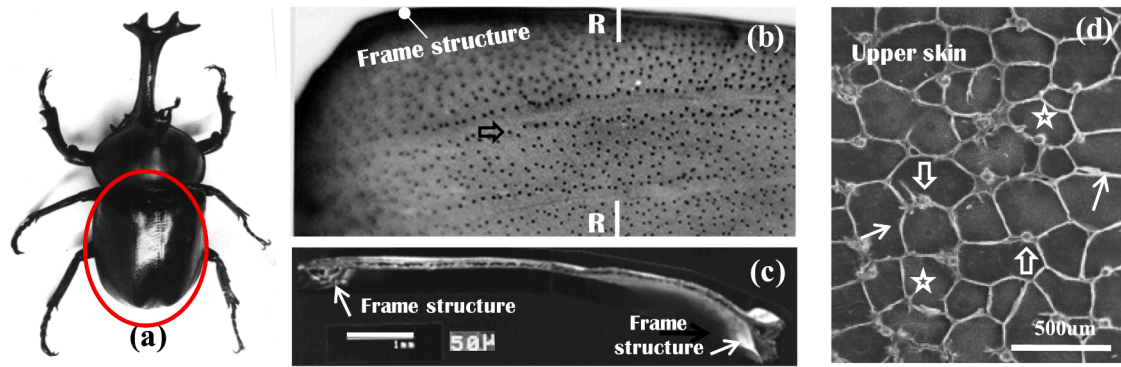

Fig. 1. Adult *Allomyrina dichotoma* beetle and the microstructure of its elytra.

instead located in the middle of the cell walls [57,60–62] BEPs can be therefore subdivided into two geometries. The first is the end-trabecular beetle elytron plate (EBEP), in which the trabeculae are placed solely at the joint of the cell walls. The second is the middle-trabecular beetle elytron plate (MBEP) [60], which has the trabeculae located in the middle of the cell walls.

Both the EBEP- and the MBEP-inspired structures made of different materials have shown clear advantages in terms of compressive properties and energy absorption capabilities compared to classical honeycomb plates, and this has been confirmed by experiments and finite element (FE) simulations [63–65]. Chiral and hierarchical honeycombs with configurations similar to the BEP topologies also show some excellent mechanical properties, as demonstrated by analytical and numerical simulations [66–68]. Three-point and cantilever sandwich beams with BEP cores subjected to bending also exhibit increased ductility compared to analogous configuration with honeycombs [69,70]. The response of a BEP structure under different types of load however depends on the equivalent elastic and nonlinear properties of the core [71–74]. To the best of the Authors' knowledge, no comprehensive study of the engineering elastic moduli of EBEPs and MBEPs has

been performed so far. In this work, we investigate the in-plane tensile modulus, Poisson's ratio and shear modulus of both EBEP and MBEP cores. The investigation is carried out using a numerical parametric analysis benchmarked by experiments. BEP cores are also compared to classical hexagonal honeycomb configurations. The numerical analysis is performed using Representative Volume Elements (RVE) models with Periodic boundary conditions (PBCs), followed by volumetric homogenization. Simulations on full scale models have also been performed to cross-validate the RVE results. Finally, uniaxial and off-axis 45° tensile tests have been performed to validate the numerical results.

2. Materials and methods

2.1. Geometry

Periodic structures are characterized by the repetition of a minimum unit cell or namely, a representative volume element (RVE). Fig. 3 shows the geometries of RVEs in honeycombs (Fig. 3a), and in the BEP topologies (Fig. 3b, EBEP cores, and, Fig. 3c, MBEP cores). For the purpose of comparison, the results from the asymptotic homogenization are
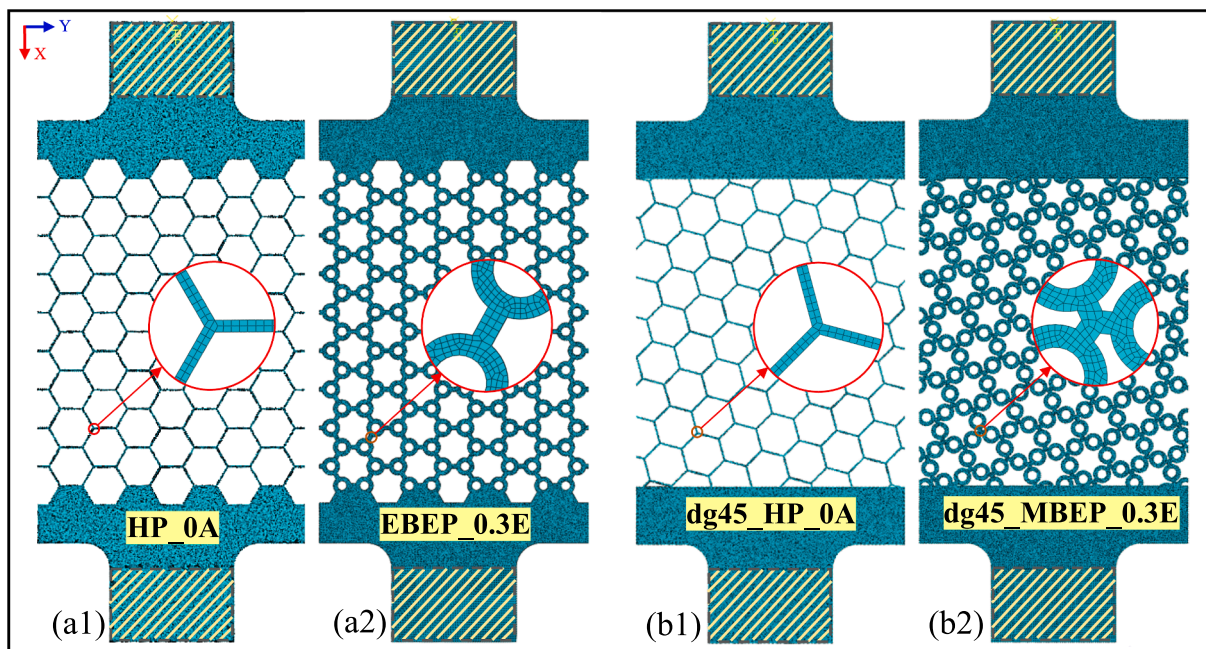

Fig. 2. Full-scale FE models. (a1) hexagonal honeycomb ($\alpha = 0, \beta = 0.067$) and (a2) EBEP configuration ($\alpha = 0.3, \beta = 0.167$) for the uniaxial tensile simulations. (b1) hexagonal honeycomb ($\alpha = 0, \beta = 0.067$) and (b2) MBEP configuration ($\alpha = 0.3, \beta = 0.167$) for the 45° off-axis tensile simulation.
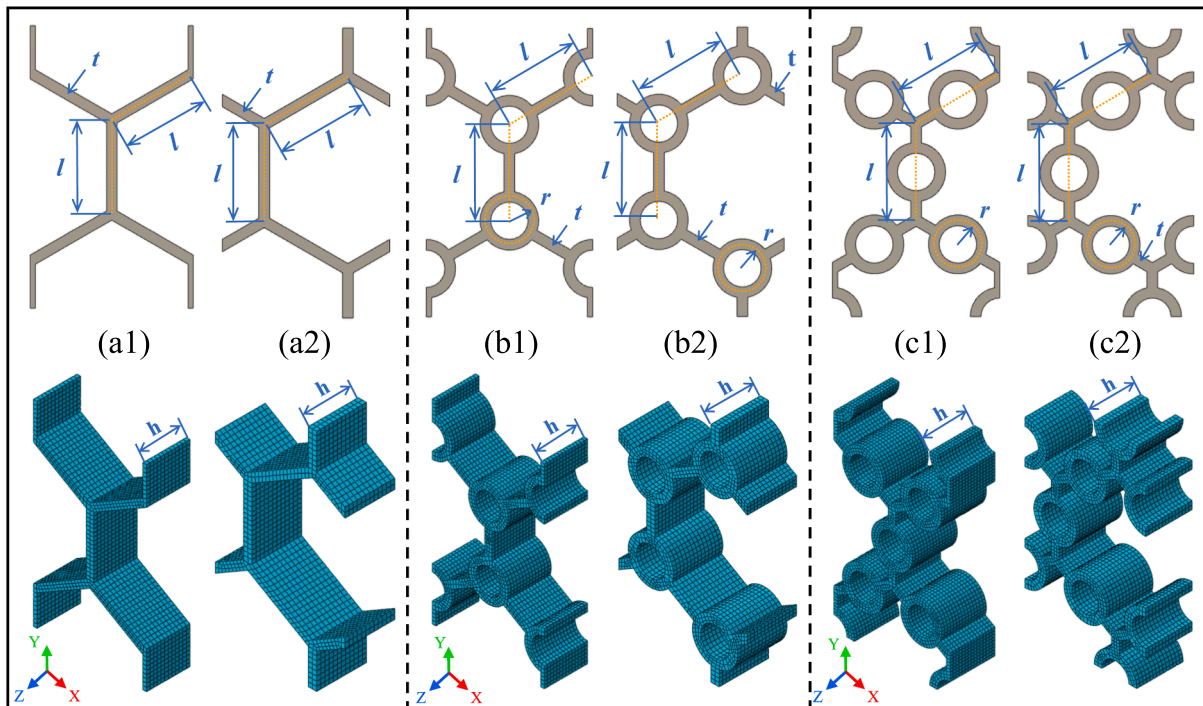
Fig. 3. Configurations of the different representative unit volumes (RVEs) in (a) honeycomb structures, (b) EBEP cores and (c) MBEP cores.

obtained from two different RVEs for the same type of core configuration (Fig. 3a1 and a2, b1 and b2, c1 and c2). All the RVEs are composed by cylinders with radius r and cell walls with length $l = 9mm$, thickness t and inclined with an angle equal to 120° between two walls (upper row in Fig. 3). The thickness of the RVE along the z-direction (lower row in Fig. 3) is indicated as h. The mechanical properties of the structures can be expressed using some nondimensional parameters like the cylindrical radius ratio $\alpha = r/l$ and the thickness ratio $\beta = t/l$ (Fig. 3). It is noticeable that not all the α and β values are admissible. For examples, the α values need to be limited within 0.5 to avoid the merging of two adjacent cylinders. The β values also are delimited when the thickness of ribs is equal to r/2, otherwise the cylinders would not be hollow. Additional parameters that characterize the mechanical behaviour of the cellular structures are the material properties of the cell walls (in-plane Young's modulus E_s, shear modulus G_c and density ρ_c in our case). In this work, we have used 5 groups of the α (α = 0, 0.1, 0.2, 0.25, 0.3) and β (β = 0.067, 0.089, 0.111, 0.133, 0.167) parameters, respectively. The hexagonal honeycomb structures have however only 5 groups of β due to the absence of cylinders in their cells, so their α values are set to zero.

Another important parameter that defines the mechanical performance of the cellular structures is the relative density ρ/ρ_c, which is defined by:

$$\frac{\rho}{\rho_c} = \frac{A}{A_c} \tag{1}$$

In (1), A is the area of solid material within a representative unit cell and A_c is the total cross-sectional area of the unit cell. Formula (1) is related to a prismatic cellular structure with constant height along the z (out-of-plane) direction. From inspection, the relative density of the EBEP configurations can be written as:

$$\frac{\rho}{\rho_c} = \frac{8}{9}\sqrt{3}\pi\alpha\beta + \frac{2}{3}\sqrt{3}\beta\left(1 - \sqrt{\beta^2 + \alpha\beta}\right) - \frac{\sqrt{3}}{3}(2\alpha + \beta)^2 \bullet \arcsin\left(\frac{\beta}{2\alpha + \beta}\right) \tag{2}$$

For the MBEP configurations, the relative density becomes:

$$\frac{\rho}{\rho_c} = \frac{4}{3}\sqrt{3}\pi\alpha\beta + \frac{2}{3}\sqrt{3}\beta\left(1 - \frac{\sqrt{3}}{3}\beta - \sqrt{\beta^2 + \alpha\beta}\right)$$
$$- \frac{\sqrt{3}}{3}(2\alpha + \beta)^2 \bullet \arcsin\left(\frac{\beta}{2\alpha + \beta}\right) \tag{3}$$

All the details of the configurations used in this article, with their names and corresponding parameters, can be found in the Appendix Figure A1 and Appendix Figure A2.

2.2. Finite element models

All the numerical models are developed using the commercial code ABAQUS 2018b. The in-plane elastic engineering properties have been simulated using full-scale representative models of the honeycomb structures and the BEP topologies. Those full-scale models provide a further benchmark to the asymptotic homogenization models represented by the RVEs with periodic boundary conditions (PBCs).

2.2.1. Full-scale representative models

Three groups of full-scale FE models representing different configurations have been prepared. The first is representative of the hexagonal honeycomb structure group with α = 0 and β = 0.067, 0.167. The second and third groups represent EBEP and MBEP configurations with α = 0.1, 0.3 and β = 0.067, 0.167, respectively. Each model has a length $l = 9mm$. The dimensions of the uniaxial and off-axis 45° tensile test samples are $251mm \times 108mm \times 3mm$. These dimensions are also adopted for the experimental specimens. Fig. 2 shows four models: two are for uniaxial tensile simulations (Fig. 2a), the others are for the 45° off-axis tensile loading (Fig. 2b). The full-size representative volumes have 77 unit cells; this figure is consistent with the minimum cell numbers recommended by the ASTM C365/C365M-16 standard. After a mesh convergence analysis, a discretization with at least two through-the-thickness elements has been adopted by using C3D8I elements (Fig. 2a, b). For all the full-scale models, the boundary conditions have been applied to the top and bottom rectangular part (Fig. 2) along the x-direction. On the top bar, each node was subjected to a constant tensile

force (linear elastic analysis). On the bottom bar, all degrees of freedom (DOF) have been clamped. As a close approximation to the effective boundary conditions existing in the experimental tests, the degrees of freedom of the nodes belonging to the top bar subjected to the tensile force were coupled to translate together along the loading direction, while the other two translational DOFs were clamped. All the rotational degrees of freedom belonging to the top and bottom bars along the x-direction have been blocked to ensure a local stiffening effect existing in the real samples. The average tensile strains were calculated vertically and horizontally (as shown in the Appendix Figure A3), to be consistent with the experimental measurements. The total tensile stress has been calculated from the cross-sectional average of the tensile force along the loading direction of the structure.

2.2.2. RVE models

All the parametrical dimensions of RVEs shown in Fig. 3 have been created with the Fusion360 CAD software, and then incorporated into ABAQUS 2018b separately. Meshes are generated using C3D8I elements, with two to three elements along the wall thickness t and maintaining a constant square aspect ratio. Considering that the honeycombs and the BEP cores are periodic structures with two planes of symmetry in the transverse and ribbon directions, the numerical analysis can become more tractable using periodic RVE models to calculate the engineering elastic properties. In this work, the modelling strategy applied to the RVEs involves the volumetric homogenization and the application of Periodic Boundary Conditions (PBCs) at the RVE boundaries.

The PBCs used in this work are strain-controlled boundary conditions that provide equal strain fields to the RVE boundaries ($\partial\Phi_{RVE}$). PBCs are implemented in ABAQUS/Standard by using linear constraint equations in Python [75,76]. The mesh nodes are constrained with different equations, depending on their position on the $\partial\Phi_{RVE}$ at vertices, edges and faces to avoid kinematic over-constraining in nodes that belong to more than surface, i.e., vertex and edges. The displacement of opposite mesh nodes at the $\partial\Phi_{RVE}$ are coupled as follows, i.e.:

$$u_x^+ - u_x^- = \varepsilon_{ij}^0(x^+ - x^-), \forall x \in \partial\Phi_{RVE} \tag{4}$$

where x^+, x^- are the coordinates of opposite paired nodes, ε_{ij}^0 is the applied strain and u is the resulting displacement [77]. The detailed constraint equations which are used in this work can be found in [78].

The numerical homogenization approach has been used to compute the elastic engineering constants of two uniaxial moduli in the x-y plane and of the in-plane shear modulus. For each loading case, only one of the six possible independent components of the volume average strain tensor in the Cartesian 3D space $\bar{\varepsilon}$ is assigned with a unit value different from zero. The homogenization technique assumes that the strain (ε_{ij}^0) applied to the RVE boundaries ($\partial\Phi_{RVE}$) is equal to the volume average strain ($\bar{\varepsilon}_{ij}$) inside the RVE:

$$\bar{\varepsilon}_{ij} = \frac{1}{V_{RVE}} \int_{V_{EFF}} \varepsilon_{ij}dV = \varepsilon_{ij}^0, \forall i,j = 1,2,3 \tag{5}$$

In (5), V_{RVE} is the volume of the RVE and V_{EFF} is the volume of the honeycomb or the BEP core unit [77].

The stiffness matrix $C_{6\times6}$ of the RVE 3D homogenized material is populated column by column with the volume-averaged stress components $\bar{\sigma}$, based on the relationship below:

$$\bar{\sigma}_\alpha = C_{\alpha\beta}\bar{\varepsilon}_\beta, where\alpha, \beta = 1, \cdots, 6. \tag{6}$$

Each column of the stiffness matrix corresponds to one static analysis. The volume-averaged stresses are calculated in the Gauss points within each solid element for each of the six loading cases [77]:

$$C_{\alpha\beta} = \bar{\sigma}_\alpha = \frac{1}{V_{RVE}} \int_{V_{EFF}} \sigma_\alpha dV = \frac{1}{V_{RVE}} \sum_{el=1}^{N} \sigma_\alpha^{el} V^{el}, when\bar{\varepsilon}_\beta = 1. \tag{7}$$

The values of the in-plane tensile moduli E_1, E_2, shear modulus G_{12} and Poisson's ratios ν_{12}, ν_{21} have been calculated from the compliance matrix S, which is the inversion of the stiffness matrix [79,80]:

$$S = \begin{bmatrix} \dfrac{1}{E_1} & -\dfrac{\nu_{12}}{E_2} & -\dfrac{\nu_{13}}{E_3} & 0 & 0 & 0 \\[2mm] -\dfrac{\nu_{21}}{E_1} & \dfrac{1}{E_2} & -\dfrac{\nu_{23}}{E_3} & 0 & 0 & 0 \\[2mm] -\dfrac{\nu_{31}}{E_1} & -\dfrac{\nu_{32}}{E_2} & \dfrac{1}{E_3} & 0 & 0 & 0 \\[2mm] 0 & 0 & 0 & \dfrac{1}{G_{23}} & 0 & 0 \\[2mm] 0 & 0 & 0 & 0 & \dfrac{1}{G_{13}} & 0 \\[2mm] 0 & 0 & 0 & 0 & 0 & \dfrac{1}{G_{12}} \end{bmatrix} \tag{8}$$

2.3. Manufacturing and experimental tests

As shown in Fig. 4, specimens have been produced using a laser cutting facility to pattern the PMMA panels (Trotec Laser Speedy 360 laser cutter with a 100 W sealed CO_2 laser). During the cutting progress, to reduce thermal residual stresses in samples, the speed is set up as 1.0 mm/s. We also use vector ordering to minimize the number of laser beam passes. Fig. 4a1 and b1 are indicative of the samples of the honeycomb configurations; Figs. a2 and b2, a3 and b3 show the EBEP and MBEP cores, respectively. The mechanical properties of the PMMA material have been determined following the ASTM D638-14 standard and using a Shimadzu Machine (1 kN load cell, 1 mm/min) on dog-bone specimens (Type I, T = 3 mm). The PMMA specimens show a Young's modulus of 3.26 ± 0.08GPa and a Poisson's ratio $\nu = 0.42 \pm 0.02$. The CAD models of the specimens shown in Fig. 4 have been created using Fusion360 and then exported to the laser cutter considering a kerf of 0.1 mm. The dimensions of each sample have a length $l = 9mm$, with $\alpha = 0$ (Fig. 4a1 and b1), 0.1 (top row in Fig. 4a2 and a3, b2 and b3) or 0.3 (bottom row in Fig. 4a2 and a3, b2 and b3) and $\beta = 0.067$ (left column in Fig. 4a2 and a3, b2 and b3) or 0.167 (right column in Fig. 4a2 and a3, b2 and b3). The dimensions of the uniaxial tensile test samples are $251mm \times 108mm \times 3mm$(Fig. 4a). An off-axis 45° tensile test has also been performed to determine the homogenized in-plane shear modulus, following the ASTM D3518/D3518M-18 standard. The dimensions of the shear test samples are the same as those of the uniaxial test specimens (Fig. 4b). The in-plane tensile tests have been performed using a Shimadzu test machine with a 1 kN load cell and a constant displacement rate of 1 mm/min (Fig. 4a4 and b4). An Imetrum video gauge system has been used to track the strain along the loading and the transverse directions.

The incremental Poisson's ratio definition is used in this work [81]:

$$\nu_{12} = -\frac{\varepsilon_2}{\varepsilon_1} \tag{9}$$

The in-plane tensile modulus is calculated according to ASTM D638-14 as follows:

$$E_1 = \frac{P_1}{bh\varepsilon_1} \tag{10}$$

The in-plane shear modulus is calculated from the following expression according to ASTM D3518/D3518M-18:

$$G_{12} = \frac{P_1}{2bh(\varepsilon_1 - \varepsilon_2)} \tag{11}$$

in which b and h are the width and the thickness of the laser-cutting samples. The loading force is P_1, ε_1 and ε_2 are the strains along loading

(x-direction) and transverse (y-) directions. Values of $\varepsilon_1, \varepsilon_2$ are calculated in each sample from the average of strains 4, 5, 6, 7 and strains 1, 2, 3, as shown in Appendix Figure A3a, b, respectively. We chose these edge points to calculate the strain as it resulted in less noise compared to using data from the central points.

3. Results and discussions

In this section, the in-plane engineering elastic properties of the BEP and honeycomb configurations, including the in-plane Young's modulus, Poisson's ratio and shear modulus versus the α and β parameters are described. Those results are obtained from simulations related to the RVEs and full-scale FE models, and the experimental tests. It is worth mentioning that the results related to the simulations on the two types of RVE configurations are the same. The RVE simulation results obtained from the hexagonal honeycomb structures have been verified by comparisons with the analytical results existing in open literature [82]. A general good agreement between them is observed, with errors ranging from 0.01% to 4.70%.

3.1. In-plane tensile modulus

Fig. 5a shows the results from RVE simulations and presents the nondimensional Young's modulus $E_1/E_s/(\rho/\rho_c)$ versus α. Because of the in-plane symmetry, the modulus E_2 is the same as E_1, apart from small numerical errors. The results related to the hexagonal honeycomb structures are showed within the purple area where the value of α is zero. The results ascribed to the EBEP and MBEP configurations are presented in the red and blue area, respectively. From the bottom to the top, each configuration has five groups of scatters, showing different cases related to the parameter β ranging from 0.067 to 0.167. From Fig. 5a, we can clearly observe an increasing trend for the nondimensional modulus E_1 versus α for the EBEP topologies, while the exact opposite occurs for the MBEP configurations. The cylinders placed at the joints of the cell walls in the EBEP cores appear to provide an increased resistance to the in-plane tensile deformation. As the cylinder becomes bigger in EBEP cores, the connecting rib becomes shorter. The significant increase of the tensile modulus of EBEP cores is thus caused by the greater bending resistance provided by both larger cylinders and shorter ribs. On the contrary, the MBEP cores that feature the hollow cylinders in the middle of the walls show a lower in-plane tensile modulus, even when compared to the classical hexagonal configurations without those
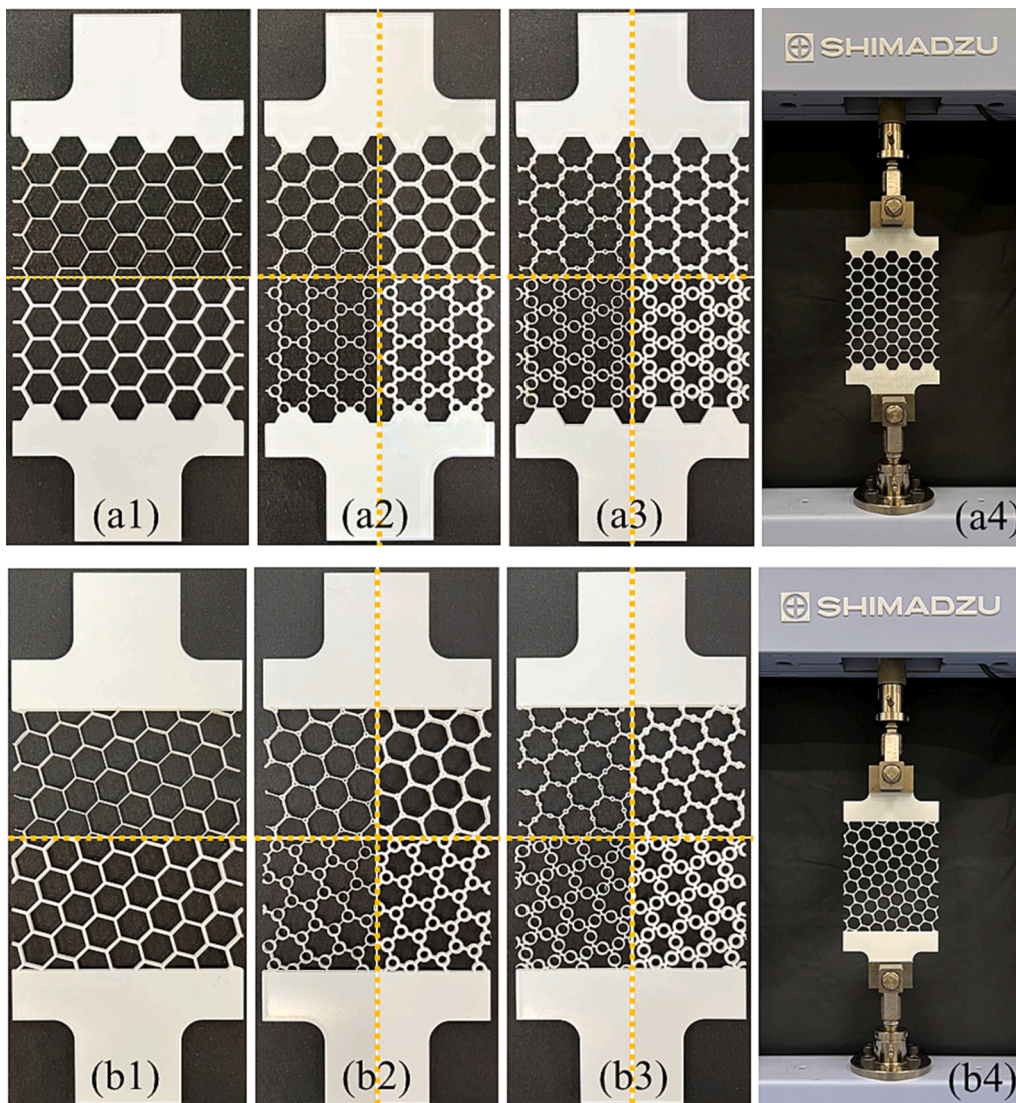

Fig. 4. Experimental samples for the uniaxial tensile test (a) and off-axis 45° tensile test (b). (a1) and (b1) are honeycomb structures; (a2) and (b2), (a3) and (b3) are configurations of the EBEP and MBEP cores, respectively. (a4) and (b4) show the Shimadzu test machine used in this work.
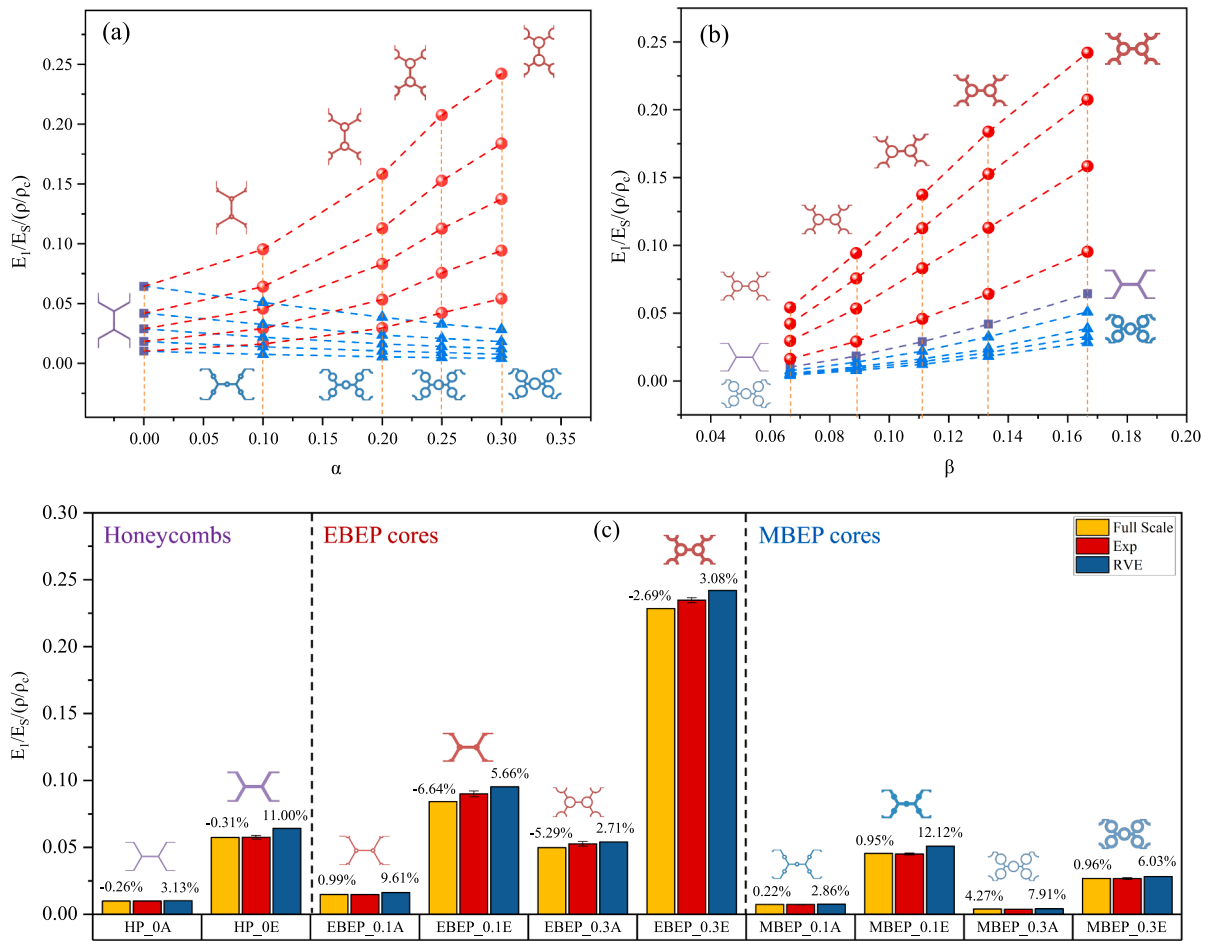
Fig. 5. Nondimensional in-plane Young's modulus versus the unit cell geometry parameters α (a) and β (b) from RVE simulations; (c) shows comparison between numerical results from RVE, full-scale models and experimental results. The numbers above the columns related to the full-scale and RVE FE results show the error between those values and the experimental ones.

cylinders.

Fig. 6 shows the deformed shapes from the full-scale simulations of the hexagonal lattice and the BEP configurations. The hexagonal lattice with the thickest cell walls ($\beta = 0.167$) and the BEP configurations with the largest cylinders ($\alpha = 0.3$), as well as the thickest cell walls are chosen as examples (Fig. 6a1, b1 and c1). Fig. 6a2, b2 and c2 show the deformed and initial shapes of the central unit cell from each configuration. The undeformed unit cells are indicated using red dash lines. The deformation factor is set as 5 in ABAQUS for all the structures. From Fig. 6a1, b1 and c1, it is evident that the cell walls of the BEP and the hexagonal honeycombs will mainly bear the load and also provide the load transfer between cells when the honeycombs are subjected to an in-plane tensile force. The load transfers from the cell walls to the end nodes of the ribs, which are represented by the cylindrical joints in the BEP honeycombs and the ends of the cell walls in the pure hexagonal configurations (Fig. 6b2, c2). In this way, the joint becomes a critical load-bearing component during the progress of the loading across the whole lattice structure. In EBEP structures (Fig. 6b2), the cylinders with the closed section located at the joints of the unit cell provide an improved torsional and tensile resistance compared to hexagonal honeycombs (Fig. 6a2) and MBEP structures (Fig. 6c2), whose joints have three open-shaped ribs tessellation at 120°. In the case of the MBEP configurations, even though cylinders are still present, their main load-bearing points are the same of those of hexagonal honeycombs;

feature makes the tensile modulus of MBEPs not exceeding the one of hexagonal honeycombs. Moreover, the cylinder distributed in the middle of cell wall provides added material to the original hexagonal cell configuration. MBEP topologies therefore show a disadvantage compared to the EBEP structures, because the position of the added cylinder does not provide the load transfer capability present in the EBEP case and the resulting increase of mass is adverse to the specific tensile stiffness.

Fig. 5b shows the nondimensional Young's modulus $E_1/E_s/(\rho/\rho_c)$ versus β obtained from the RVE simulations. The stiffness performance of the pure hexagonal structures is also contained within the purple area, while the results of the EBEP and MBEP configurations are present in the red and blue areas, respectively. The EBEP configurations are regrouped along four curves, showing different cases related to α ranging from 0.1 to 0.3; the normalized moduli increase with the increase of α. In contrast, the MEBP configuration decrease their normalized stiffness when α increases from 0.1 to 0.3. The pure hexagonal structures feature only one curve, because their α value is zero. As shown in Fig. 5b, both the hexagonal lattice and BEP structures have an increase of the nondimensional in-plane tensile modulus when the cell walls become thicker (i.e., when β increases). The thicker ribs provide stiffer constraints inside the whole cellular structure. It is worth mentioning that the dependency versus β^3 of nondimensional tensile modulus of the hexagonal honeycombs and the BEP configurations has been analysed.
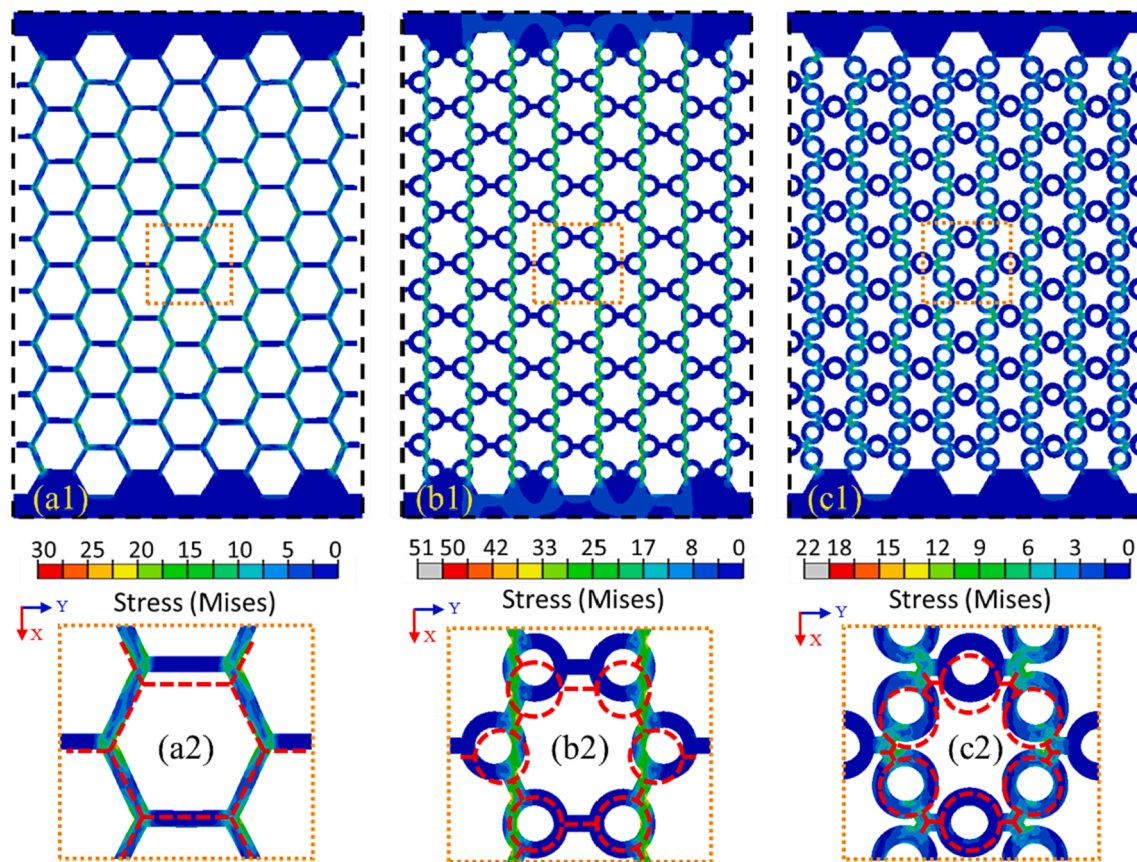
Fig. 6. Deformation diagrams from full-scale simulations on tensile modulus. (a1) HP_0E (b1) EBEP 0.3E and (c1) MBEP_0.3E. (a2), (b2), (c2) show the deformations in one unit cell.

This dependency provided information about the importance of the bending deformation mechanism of the ribs to affect the in-plane engineering constants [82,83]. Results show that the EBEP configurations show some departures from a linear proportionality when the value of the cube of β increases. This phenomenon become more obvious in the cases of larger α values. The hexagonal lattice and the MBEP configurations however show almost straight lines. The differences between them show that the presence of the cylinders in the EBEP configurations change the load-bearing configuration of the whole structure; the cylinders make the lattice configuration to resist the external tensile loading under a multi-deformation other than bending dominated deformation. For further validation, Fig. 5c shows the comparison between the results from FE simulation, with RVEs and full-scale models, and the experiments. Each group with three columns shows the results about one type of specimen. For the pure hexagonal structures, the two left groups in Fig. 5c are related to specimens with α = 0 and β = 0.067 or 0.167. For the EBEP and the MBEP structures, four specimens of each configuration with α = 0.1 or 0.3 and β = 0.067 or 0.167 are presented in Fig. 5c, respectively. In each group, the red column indicates the experimental results, while the yellow and blue ones illustrate the full-scale and RVE simulation results. The numbers above the columns of full-scale and RVE results show the error between their values and the experimental one, where the negative error reflects lower simulation values compared to the experimental ones. The opposite is true for the positive errors. It is possible to appreciate a good consistency between the full-scale simulating and the experimental results, with all the errors being below 7%. The minimum error of 0.22% is for the MBEP_0.1A group, the one with the smallest cylinders (α = 0.1) and thinnest cell

walls (β = 0.067). The EBEP and hexagonal lattice configurations that feature the same geometric parameters also exhibit similar small errors (0.3% of EBEP_0.1A and 1% of HP_0A). When we are comparing the two sets of simulations (RVE and full-scale models), it is noteworthy that most errors are under 10%, except for the three groups HP_0E (11.3%), EBEP_0.1E (12.3%) and MBEP_0.1E (11.2%). Those groups all feature the smallest cylinders (or no cylinders in the case of the hexagonal lattice), but the thickest cell walls (α = 0 or 0.1, β = 0.167). One can also observe that the EBEP, MBEP and original hexagonal honeycombs, which feature thick cell walls and small cylinders, have the tensile moduli more sensitive to the size of the models. This sensitivity causes more discrepancies between the results of RVE FE models (representing a lattice with an infinite number of unit cells), and the full-scale FE models (77 unit cells).

3.2. Poisson's ratio

Fig. 7a shows the RVE simulation results of the in-plane Poisson's ratio ν_{12} versus α. Because of the in-plane symmetry, the Poisson's ratio ν_{21} is the same as ν_{12}, except for small numerical errors. The results related to hexagonal honeycomb structures are located within the purple area where α value is zero. The Poisson's ratios of the EBEP and MBEP configurations are distributed in the red and blue areas, respectively. The values of the Poisson's ratios range between 0.36 and 0.98. Each configuration has five groups of curves related to the geometry parameter β ranging from 0.067 to 0.167. From Fig. 7a, it is possible to observe that the Poisson's ratio ν_{12} decreases versus α for the two BEP topologies, especially for the EBEP cores. When the cylinder radius is
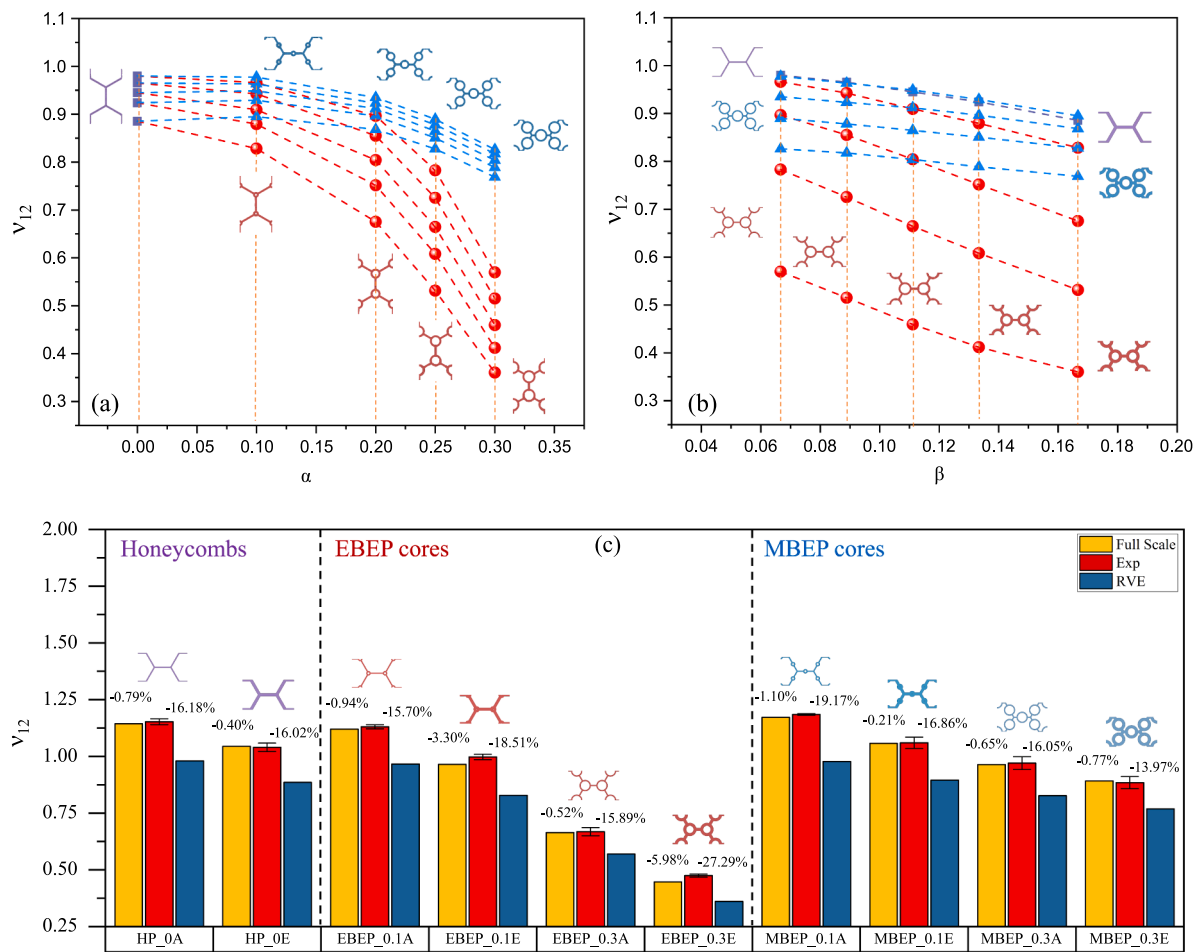
Fig. 7. In-plane Poisson's ratios versus the unit cell geometry parameters α (a) and β (b) from RVE simulations; (c) shows comparison between numerical results from RVE, full-scale models and experimental results. The numbers above the columns related to the full-scale and RVE FE results show the error between those values and the experimental ones.

small, the stress distribution within the EBEP core under tension is similar to the hexagonal honeycomb structure, as shown in Fig. 6a1. However, when the size of the cylinder becomes large, the force line tends to become straight (see the green lines in Fig. 6b1). It is known that the Poisson's ratio for a straight (rectangular honeycomb) is virtually 0, so compared with the EBEP core that has smaller cylinders (Fig. 6a1), the core with larger cylinders (Fig. 6b1) will have a Poisson's ratio that is closer to 0. The EBEP configurations show however a higher sensitivity versus α compared to the MBEP structures; the latter have a more stable Poisson's ratios behaviour against the r/l ratio. The different performance of the two cellular with the cylinders is again caused by the relative locations of the same cylinders. The EBEP configurations show the broader range of available Poisson's ratios (between 0.36 and 0.97). The above-mentioned differences in terms of effects of the cylinders provide the EBEP structures with a larger set of possible mechanical properties, while the MBEP configurations have a narrower design space in terms of Poisson's ratios (between 0.77 and 0.98). It is worth of notice that the hexagonal configurations with no cylinders feature the narrowest range of Poisson's ratios (0.89–0.99 for the range of β considered in this work – Fig. 7b).

Fig. 7b shows the results of in-plane Poisson's ratio ν_{12} versus β from RVE simulations. The hexagonal lattice structures have only one curve, with α equals to zero. The EBEP and MBEP configurations are defined by the points corresponding to the four sets of α parameters ranging from

0.1 to 0.3. The in-plane Poisson's ratios of both the hexagonal lattices and the BEP structures are decreasing as the β value increases. Similar behaviours have been reported in the hexagonal and re-entrant honeycombs [82,84–87]. It is noteworthy that the MBEP configurations have a decreasing Poisson's ratio versus β that is like the one exhibited by the honeycomb structures, while the decreasing trends in EBEP configurations are more obvious. This also proves the aforementioned point that the properties of the whole EBEP core are significantly affected by the specific location of the cylinders, making them behave in a different manner from the baseline hexagonal lattice with no cylinders. The MBEP cores possess the same configuration of cell walls joint as the hexagonal honeycomb lattices and therefore provide a similar behaviour to the latter under comparable geometry configurations (top curve of the MBEP group compared to the hexagonal lattice one in Fig. 7b).

Fig. 7c shows the comparison between the results belonging to the RVE FE and full-scale models' simulations, and the experiments. The two groups at the left show the results related to the honeycomb lattices (α = 0 and β = 0.067 and 0.167); the other groups show the corresponding results from specimens of BEPs with α = 0.1 or 0.3 and β = 0.067 or 0.167. The experimental results show higher Poisson's ratios values than those provided by the simulations, and the relative errors are larger compared to those measured for the tensile modulus. The differences between RVE simulations and experiments are also likely caused by the limited dimensions of the experimental specimens,
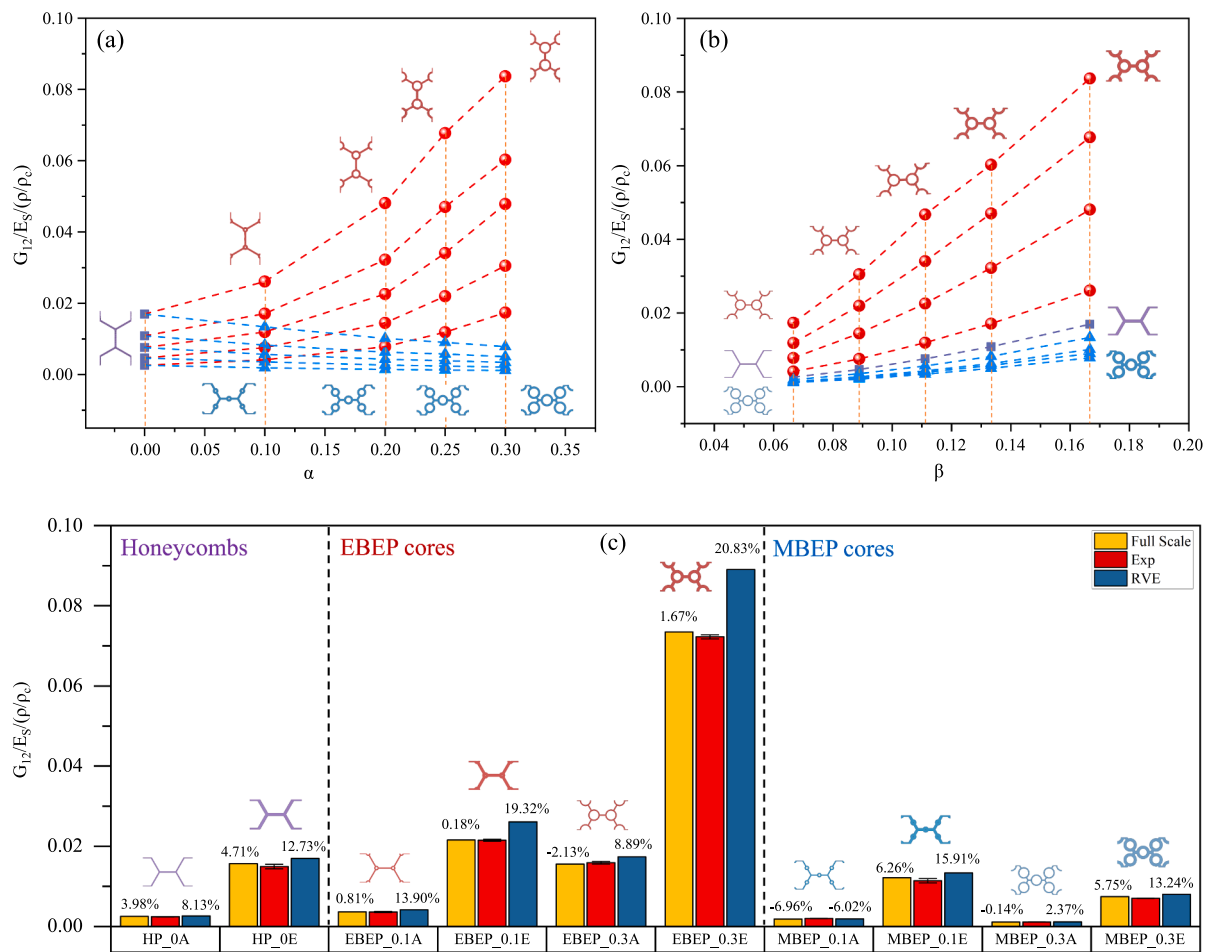
Fig. 8. Nondimensional in-plane shear modulus versus the unit cell geometry parameters α (a) and β (b) from RVE simulations; (c) shows comparison between numerical results from RVE, full-scale models and experimental results. The numbers above the columns related to the full-scale and RVE FE results show the error between those values and the experimental ones.

compared to the RVE FE models representing infinite tessellations. The size of the models however is the same for the full-scale simulations and the experiments; the errors between them are therefore relatively low (below 6%).

3.3. In-plane shear modulus

Fig. 8a shows the results of the nondimensional in-plane shear modulus $G_{12}/E_s/(\rho/\rho_c)$ versus α from RVE simulations. The shear modulus is normalized with the Young's modulus of core material E_s and the relative density ρ/ρ_c. In this case, the geometry parameter β ranges from 0.067 to 0.167. From Fig. 8a, we can observe a similar increasing trend of the nondimensional G_{12} for larger α values in the case of the EBEP topologies; the nondimensional shear modulus of the MBEP structures is however decreasing for increasing α values. Fig. 9 shows the deformation shapes from the full-scale simulations of the hexagonal lattice and the BEP configurations. The deformed and initial shapes of the central unit cell from each configuration are present in Fig. 9a2, b2 and c2. The deformation factor is set as 5 in ABAQUS for all the structures. The reason behind the different behaviours between the EBEP and the MBEP configurations is similar to the one observed in the case of the in-plane tensile modulus (see section 3.1): the cylinders of the EBEPs are located in key load-bearing positions of the unit cell (Fig. 9b2) and they

provide a larger resistance to in-plane torsion than the simple three cell walls connected at the joint, typical of the hexagonal lattice (Fig. 9a2) and the MBEP configurations (Fig. 9c2).

Fig. 8b shows the nondimensional in-plane shear modulus $G_{12}/E_s/(\rho/\rho_c)$ versus β extracted from RVE simulations. The curves related to the EBEP and MBEP configurations are ordered as four groups, according to the α values. From Fig. 8b, it is evident that the nondimensional in-plane shear modulus increases when the thickness of the cell walls increases, both for the hexagonal lattice and the BEP structures. Fig. 8c shows the comparison between the results from FE simulations with the RVE (blue columns), full-scale models (yellow columns) and the experiments (red columns). Also in this case, the comparison is based on the two types of hexagonal lattice (with α = 0 and β = 0.067 or 0.167) and four specimens (with α = 0.1 or 0.3 and β = 0.067 or 0.167) of the EBEP and MBEP cores, respectively. From Fig. 8c, it is possible to notice a good consistency between the full-scale simulations and the experimental results, with all the errors being below 7%. Nevertheless, the differences between the RVE simulations and the experiments tend to be larger than those between the full-scale simulations and tests. Similar to the datasets related to the tensile modulus, all the configurations with the thickest cell walls (β = 0.167) show relatively larger differences between the RVE simulations and the experimental results, compared to those with the thinnest cell walls.
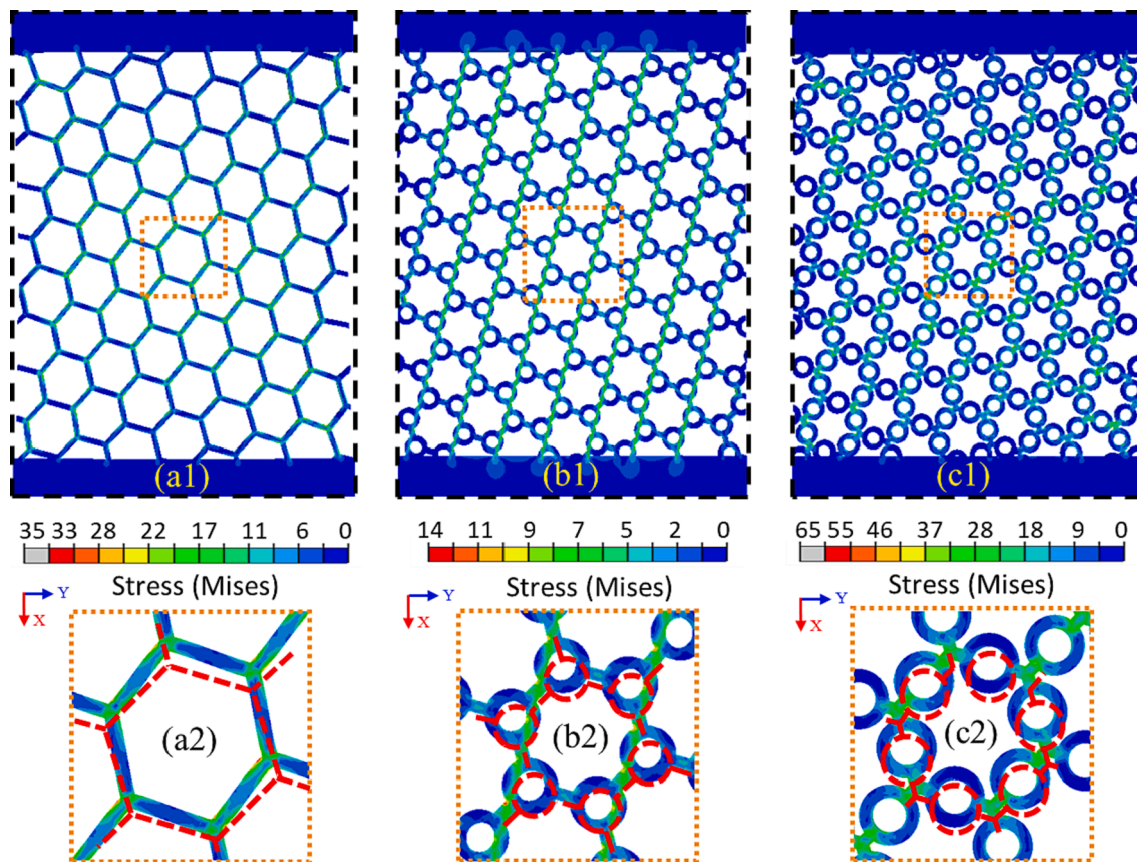
Fig. 9. Deformation diagrams from full-scale simulations on in-plane shear modulus. (a1) HP_0E (b1) EBEP 0.3E and (c1) MBEP_0.3E. (a2), (b2), (c2) show the deformations in one unit cell.

4. Conclusions

In this work, the in-plane nondimensional engineering elastic constants of both end- and middle-trabecular beetle elytron plate cores are investigated by performing a parametric analysis via experiments and numerical techniques. In addition, the comparison between BEP cores and classical hexagonal honeycomb structures is also presented. The numerical analysis has been performed using Representative Volume Elements (RVE) models of BEPs and honeycomb topologies with Periodic boundary conditions (PBCs) and volumetric homogenization. Each RVE model has been simulated using two types of cell tessellations for cross-benchmark. Furthermore, simulations on full-scale models have also been performed to be compared against the RVE simulations. Uniaxial and off-axis 45° tensile tests have also been conducted to further validate the numerical results. The data show that the in-plane nondimensional tensile modulus of the EBEPs raise significantly as the size of the cylinder increases, while the modulus of the MBEP cores slowly drops. Although both MBEP and EBEP cores have hollow cylinders in their unit cells, the cylinders in EBEP cores are located at the joints of cell walls; their torsional and tensile resistance can be fully performed because the joints are critical points for load bearing. In the case of MBEP configurations, their main load-bearing points are the same of those of the hexagonal honeycombs. Moreover, their cylinders cause extra material compared to the original hexagonal lattice. As a result, MBEP topologies show a disadvantage related to the tensile modulus under comparison with the EBEP structures. The Poisson's ratios of the EBEP cores show a high sensitivity versus the geometry parameters α

and β, while those of the MBEP cores are less affected by the variation of the cell geometry. The position of the cylinders in the EBEP structures is key to provide the load-transfer capabilities that affect the properties of the whole lattice structure. As the dimensions of the cylinders increase, the stiffness of lattice gradually grows higher from the one of the baseline pure hexagonal configurations, thus making the mechanical properties of the EBEP cores more sensitive to the geometry parameters.

Declaration of Competing Interest

The authors declare that they have no known competing financial interests or personal relationships that could have appeared to influence the work reported in this paper.

Data availability

The raw/processed data required to reproduce these findings cannot be shared at this time as the data also forms part of an ongoing study.
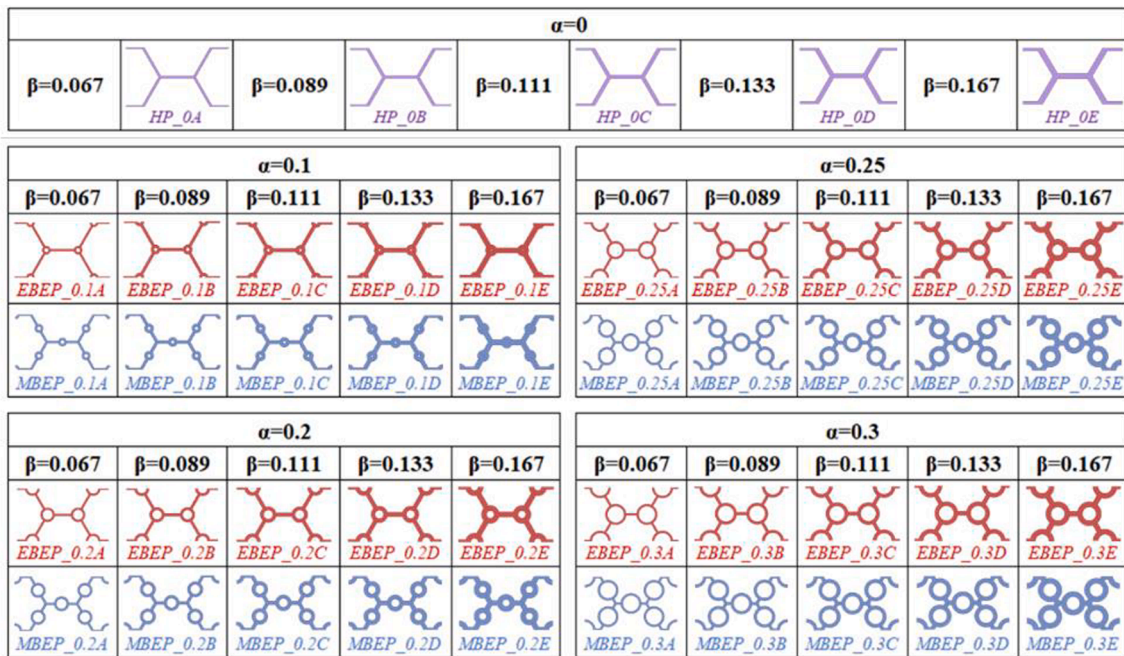
Appendix

Figure A1. Names and configurations (type 1) of RVEs with different geometry parameters.
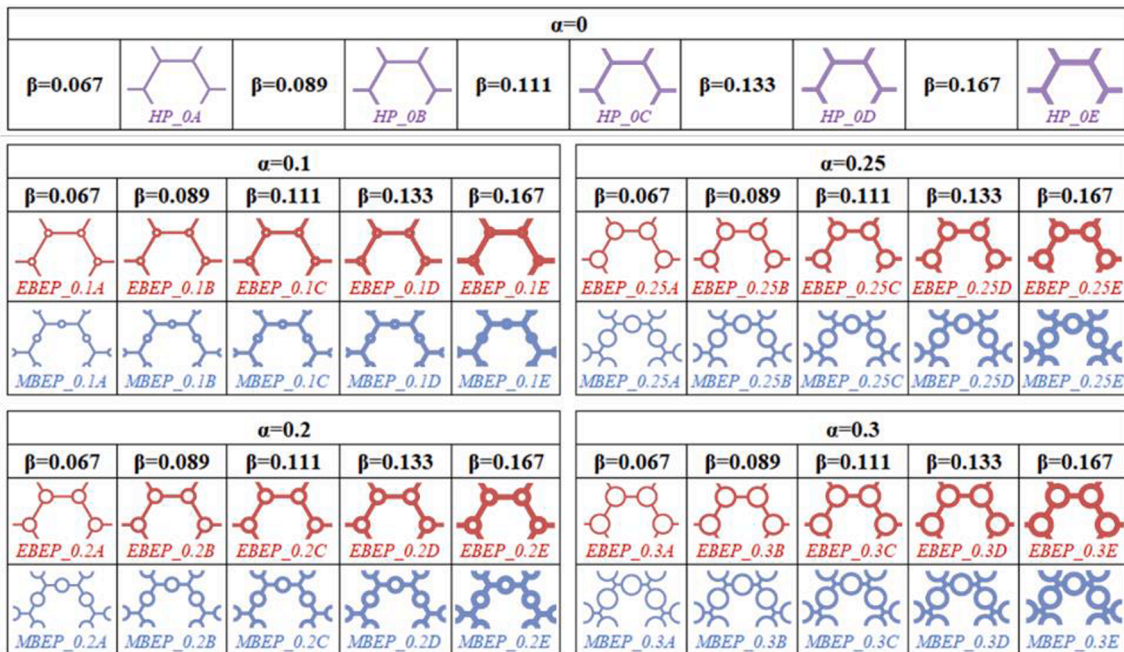

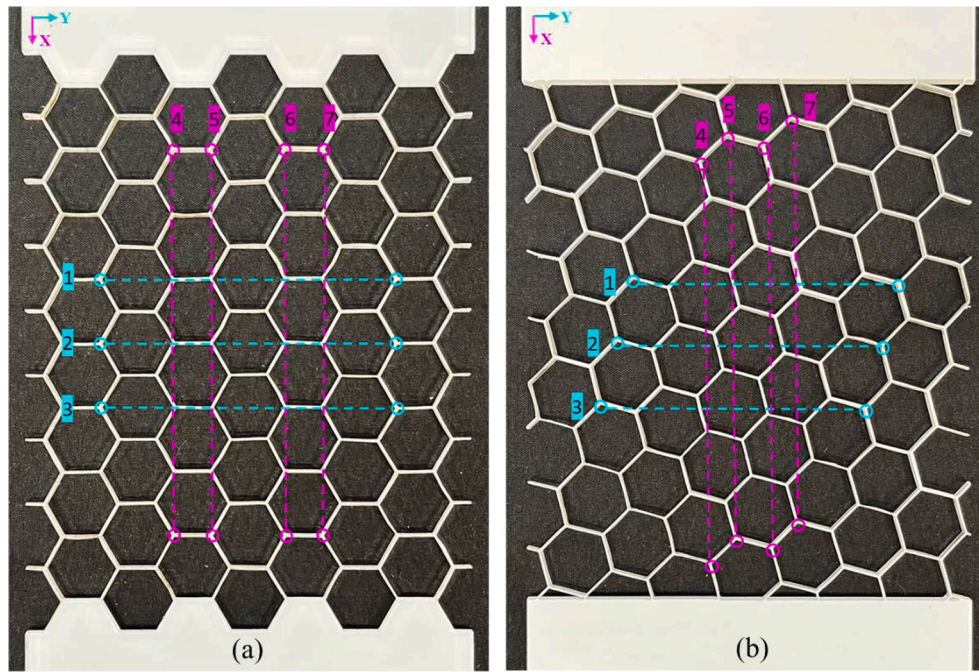**Figure A2.** Names and configurations (type 2) of RVEs with different geometry parameters.

Figure A3. strain measurements for uniaxial (a) and 45° off-axis (b) tensile simulations (full-scale) and experiments.

References

[1] H. G. ALLEN, "CHAPTER 1 - INTRODUCTION," in *The Commonwealth and International Library: Structures and Solid Body Mechanics Division*, H. G. B. T.-A. and D. of S. S. P. ALLEN, Ed. Pergamon, 1969, pp. 1–7.

[2] Hou Y, Tai YH, Lira C, Scarpa F, Yates JR, Gu B. The bending and failure of sandwich structures with auxetic gradient cellular cores. Compos Part A Appl Sci Manuf 2013;49:119–31. https://doi.org/10.1016/j.compositesa.2013.02.007.

[3] Imbalzano G, Linforth S, Ngo TD, Lee PVS, Tran P. Blast resistance of auxetic and honeycomb sandwich panels: comparisons and parametric designs. Compos Struct Jan. 2018;183(1):242–61. https://doi.org/10.1016/J.COMPSTRUCT.2017.03.018.

[4] Arunkumar MP, Pitchaimani J, Gangadharan KV, Lenin Babu MC. Sound transmission loss characteristics of sandwich aircraft panels: influence of nature of core. J Sandw Struct Mater 2017;19(1):26–48. https://doi.org/10.1177/1099636216652580.

[5] Taylor EA, Glanville JP, Clegg RA, Turner RG. Hypervelocity impact on spacecraft honeycomb: hydrocode simulation and damage laws. Int J Impact Eng 2003;29(1):691–702. https://doi.org/10.1016/j.ijimpeng.2003.10.016.

[6] Xiao Y, Hu Y, Zhang J, Song C, Huang X, Yu J, et al. The bending responses of sandwich panels with aluminium honeycomb core and CFRP skins used in electric vehicle body. Adv Mater Sci Eng 2018:1–11. https://doi.org/10.1155/2018/5750607.

[7] Tabatabaiefar HR, Mansoury B, Javad M, Zand K, Potter D. Mechanical properties of sandwich panels constructed from polystyrene/cement mixed cores and thin cement sheet facings. J Sandw Struct Mater 2017;19(4):456–81. https://doi.org/10.1177/1099636215621871.

[8] Chróścielewski J, Miśkiewicz M, Pyrzowski Ł, Sobczyk B, Wilde K. A novel sandwich footbridge - practical application of laminated composites in bridge design and in situ measurements of static response. Compos Part B Eng 2017;126:153–61. https://doi.org/10.1016/j.compositesb.2017.06.009.

[9] De C, Muscat-Fenech M, Cortis J, Cassar C. Impact damage testing on composite marine sandwich panels, part 1: quasi-static indentation. J Sandw Struct Mater 2014;16(4):341–76. https://doi.org/10.1177/1099636214529959.

[10] Allen T, Battley M. Estimation of transverse shear force during slamming impacts on a simply supported composite panel using a strain derivative method. Compos Struct 2016;153:42–9. https://doi.org/10.1016/j.compstruct.2016.06.001.

[11] Manteghi S, Mahboob Z, Fawaz Z, Bougherara H. Investigation of the mechanical properties and failure modes of hybrid natural fiber composites for potential bone fracture fixation plates. J Mech Behav Biomed Mater 2017;65:306–16. https://doi.org/10.1016/j.jmbbm.2016.08.035.

[12] Lillie EM, Urban JE, Lynch SK, Weaver AA, Stitzel JD. Evaluation of skull cortical thickness changes with age and sex from computed tomography scans: skull cortical thickness changes with age and sex from CT scans. J Bone Miner Res 2016;31(2):299–307.

[13] Karahan M, Karahan N. Development of an innovative sandwich composites for the protection of lower limbs against landmine explosions. J Reinf Plast Compos 2016;35(24):1776–91.

[14] Scarpa F, Ciffo LG, Yates JR. Dynamic properties of high structural integrity auxetic open cell foam. Smart Mater Struct 2004;13(1):49–56. https://doi.org/10.1088/0964-1726/13/1/006.

[15] Sun G, Wang E, Wang H, Xiao Z, Li Q. Low-velocity impact behaviour of sandwich panels with homogeneous and stepwise graded foam cores. Mater Des 2018;160:1117–36. https://doi.org/10.1016/j.matdes.2018.10.047.

[16] Shunmugasamy VC, Mansoor B. Aluminum foam sandwich with density-graded open-cell core: compressive and flexural response. Mater Sci Eng A 2018;731:220–30. https://doi.org/10.1016/j.msea.2018.06.048.

[17] Yaseer Omar M, Xiang C, Gupta N, Strbik OM, Cho K. Syntactic foam core metal matrix sandwich composite: compressive properties and strain rate effects. Mater Sci Eng A 2015;643:156–68. https://doi.org/10.1016/j.msea.2015.07.033.

[18] Arunkumar MP, Pitchaimani J, Gangadharan KV. Bending and free vibration analysis of foam-filled truss core sandwich panel. Jnl of Sandwich Struct Mater 2018;20(5):617–38.

[19] Xu J, Wu Y, Wang L, Li J, Yang Y, Tian Y, et al. Compressive properties of hollow lattice truss reinforced honeycombs (Honeytubes) by additive manufacturing: patterning and tube alignment effects. Mater Des 2018;156:446–57. https://doi.org/10.1016/j.matdes.2018.07.019.

[20] Chiras S, Mumm DR, Evans AG, Wicks N, Hutchinson JW, Dharmasena K, et al. The structural performance of near-optimized truss core panels. Int J Solids Struct 2002;39(15):4093–115. https://doi.org/10.1016/S0020-7683(02)00241-X.

[21] Hou Y, Neville R, Scarpa F, Remillat C, Gu B, Ruzzene M. Graded conventional-auxetic Kirigami sandwich structures: flatwise compression and edgewise loading. Compos Part B Eng Mar. 2014;59:33–42. https://doi.org/10.1016/j.compositesb.2013.10.084.

[22] Balcı O, Çoban O, Bora MÖ, Akagündüz E, Yalçin EB. Experimental investigation of single and repeated impacts for repaired honeycomb sandwich structures. Mater Sci Eng A 2017;682:23–30. https://doi.org/10.1016/j.msea.2016.11.030.

[23] Imbalzano G, Tran P, Ngo TD, Lee PV. Three-dimensional modelling of auxetic sandwich panels for localised impact resistance. J Sandw Struct Mater 2017;19(3):291–316. https://doi.org/10.1177/1099636215618539.

[24] D. W. Thompson, *On Growth and Form.* Cambridge: Cambridge University Press, 1992.

[25] Saito K, Nomura S, Yamamoto S, Niiyama R, Okabe Y. Investigation of hindwing folding in ladybird beetles by artificial elytron transplantation and microcomputed tomography. Proc Natl Acad Sci U S A May 2017;114(22):5624–8. https://doi.org/10.1073/pnas.1620612114.

[26] Yin H, Huang X, Scarpa F, Wen G, Chen Y, Zhang C. In-plane crashworthiness of bio-inspired hierarchical honeycombs. Compos Struct 2018;192:516–27. https://doi.org/10.1016/j.compstruct.2018.03.050.

[27] Ullah I, Elambasseril J, Brandt M, Feih S. Performance of bio-inspired Kagome truss core structures under compression and shear loading. Compos Struct 2014;118:294–302. https://doi.org/10.1016/j.compstruct.2014.07.036.

[28] Djumas L, Molotnikov A, Simon GP, Estrin Y. Enhanced mechanical performance of bio-inspired hybrid structures utilising topological interlocking geometry. Sci Rep 2016;6(1):26706. https://doi.org/10.1038/srep26706.

[29] Tasdemirci A, Akbulut EF, Guzel E, Tuzgel F, Yucesoy A, Sahin S, et al. Crushing behavior and energy absorption performance of a bio-inspired metallic structure: experimental and numerical study. Thin-Walled Struct 2018;131:547–55. https://doi.org/10.1016/j.tws.2018.07.051.

[30] Abo Sabah SH, Kueh ABH, Al-Fasih MY. Comparative low-velocity impact behavior of bio-inspired and conventional sandwich composite beams. Compos Sci Technol 2017;149:64–74. https://doi.org/10.1016/j.compscitech.2017.06.014.

[31] Fan X, Verpoest I, Vandepitte D. Finite element analysis of out-of-plane compressive properties of thermoplastic honeycomb. J Sandw Struct Mater 2006;8 (5):437–58. https://doi.org/10.1177/1099636206065862.

[32] Han B, Qin K, Yu B, Wang B, Zhang Q, Lu TJ. Honeycomb–corrugation hybrid as a novel sandwich core for significantly enhanced compressive performance. Mater Des 2016;93:271–82. https://doi.org/10.1016/j.matdes.2015.12.158.

[33] Sun G, Huo X, Chen D, Li Q. Experimental and numerical study on honeycomb sandwich panels under bending and in-panel compression. Mater Des 2017;133: 154–68. https://doi.org/10.1016/j.matdes.2017.07.057.

[34] Yu B, Han B, Su P-B, Ni C-Y, Zhang Q-C, Lu TJ. Graded square honeycomb as sandwich core for enhanced mechanical performance. Mater Des 2016;89:642–52. https://doi.org/10.1016/j.matdes.2015.09.154.

[35] Jung W-Y, Aref AJ. A combined honeycomb and solid viscoelastic material for structural damping applications. Mech Mater 2003;35(8):831–44. https://doi.org/10.1016/S0167-6636(02)00210-7.

[36] Zhou X, Yu D, Zhang S. Homogenous asymptotic analysis on vibration energy dissipation characteristics of periodical honeycomb reinforced composite laminate filled with viscoelastic damping material. Compos Struct 2021;258:113307. https://doi.org/10.1016/j.compstruct.2020.113307.

[37] Hyungoo K, Jinkoo K. Damage mitigation of a steel column subjected to automobile collision using a honeycomb panel. J Perform Constr Facil Feb. 2020; 34(1):4019107. https://doi.org/10.1061/(ASCE)CF.1943-5509.0001394.

[38] Sun G, Jiang H, Fang J, Li G, Li Q. Crashworthiness of vertex based hierarchical honeycombs in out-of-plane impact. Mater Des 2016;110:705–19. https://doi.org/10.1016/j.matdes.2016.08.032.

[39] Horrigan DPW, Staal RA. Predicting failure loads of impact damaged honeycomb sandwich panels - a refined model. J Sandw Struct Mater Oct. 2010;13(1):111–33. https://doi.org/10.1177/1099636208105039.

[40] Cheng S, Qiao P, Chen F. Numerical analysis of I-Lam honeycomb sandwich panels for collision protection of reinforced concrete beams. J Sandw Struct Mater Jan. 2016;19(4):497–522. https://doi.org/10.1177/1099636215623816.

[41] F. Luo, S. Zhang, and D. Yang, "Anti-Explosion Performance of Composite Blast Wall with an Auxetic Re-Entrant Honeycomb Core for Offshore Platforms," *Journal of Marine Science and Engineering* , vol. 8, no. 3. 2020, doi: 10.3390/jmse8030182.

[42] A. S. Herrmann, P. C. Zahlen, and I. Zuardy, "Sandwich Structures Technology in Commercial Aviation BT - Sandwich Structures 7: Advancing with Sandwich Structures and Materials," 2005, pp. 13–26.

[43] Crupi V, Epasto G, Guglielmino E. Comparison of aluminium sandwiches for lightweight ship structures: honeycomb vs. foam. Mar Struct 2013;30:74–96. https://doi.org/10.1016/j.marstruc.2012.11.002.

[44] Shen W, Luo B, Yan R, Zeng H, Xu L. The mechanical behavior of sandwich composite joints for ship structures. Ocean Eng 2017;144:78–89. https://doi.org/10.1016/j.oceaneng.2017.08.039.

[45] Wang J, Shi C, Yang N, Sun H, Liu Y, Song B. Strength, stiffness, and panel peeling strength of carbon fiber-reinforced composite sandwich structures with aluminum honeycomb cores for vehicle body. Compos Struct 2018;184:1189–96. https://doi.org/10.1016/j.compstruct.2017.10.038.

[46] Zhao C, Zhao Y, Ma J. The stability of new single-layer combined lattice shell based on aluminum alloy honeycomb panels. Appl Sci 2017;7(11):1150. https://doi.org/10.3390/app7111150.

[47] Magnucki K. Bending of symmetrically sandwich beams and I-beams – Analytical study. Int J Mech Sci 2019;150:411–9. https://doi.org/10.1016/j.ijmecsci.2018.10.020.

[48] Kirejtshuk AG, Poschmann M, Prokop J, Garrouste R, Nel A. Evolution of the elytral venation and structural adaptations in the oldest Palaeozoic beetles (Insecta: Coleoptera: Tshekardocoleidae). J Syst Palaeontol Jul. 2014;12(5):575–600. https://doi.org/10.1080/14772019.2013.821530.

[49] Sun J, Wu W, Song Z, Tong J, Zhang S. Bio-inspirations for the Development of Light Materials based on the Nanomechanical Properties and Microstructures of Beetle Dynastes tityus. J Bionic Eng 2019;16(1):154–63. https://doi.org/10.1007/s42235-019-0014-7.

[50] Noh MY, Muthukrishnan S, Kramer KJ, Arakane Y. Development and ultrastructure of the rigid dorsal and flexible ventral cuticles of the elytron of the red flour beetle, Tribolium castaneum. Insect Biochem Mol Biol Dec. 2017;91:21–33. https://doi.org/10.1016/j.ibmb.2017.11.003.

[51] Chen J, Ni Q. Three dimensional composite structures in the fore-wing of beetles. Acta Materiae Compositae Sinica 2003;20(6):61–6. In Chinese.

[52] Le TQ, Truong TV, Tran HT, Park SH, Ko JH, Park HC, et al. How Could Beetle's Elytra support their own weight during forward flight? J Bionic Eng 2014;11(4): 529–40. https://doi.org/10.1016/S1672-6529(14)60065-2.

[53] Linz DM, Hu AW, Sitvarin MI, Tomoyasu Y. Functional value of elytra under various stresses in the red flour beetle, Tribolium castaneum. Sci Rep 2016;6(1): 34813. https://doi.org/10.1038/srep34813.

[54] Xiang C T, "Mechanism of natural composite materials and composite materials research coleoptera insects bionic design-it's gradual microstructure and mechanical behavior," Chongqing University., 1994.

[55] Chen J, Ni QQ, Xu Y, Iwamoto M. Lightweight composite structures in the forewings of beetles. Compos Struct 2007;79(3):331–7. https://doi.org/10.1016/j.compstruct.2006.01.010.

[56] B. Chen, X. P and J. F, "MICROSTRUCTURE OF NATURAL BIOCOMPOSITES AND RESEARCH OF BIOMIMETIC COMPOSITES," Acta Materiae Compositae Sinica, vol. 17, no. 3, pp. 59–62, 2000, doi: https://doi.org/10.3321/j.issn:1000-3851.2000.03.014. (In Chinese).

[57] Chen JX. Fundamental study on biomimetics composites. Kyoto Inst Technol 2001.

[58] J. Chen and Q. Ni, "THREE DIMENSIONAL COMPOSITE STRUCTURES IN THE FORE-WING OF BEETLES," Acta Materiae Compositae Sinica, vol. 20, no. 6, pp. 61–66, doi: https://doi.org/10.3321/j.issn:1000-3851.2003.06.013. (In Chinese).

[59] Chen JX, Zhang XM, Okabe Y, Xie J, Xu MY. Beetle elytron plate and the synergistic mechanism of a trabecular-honeycomb core structure. Sci China Technol Sci 2019; 62(1):87–93. https://doi.org/10.1007/s11431-018-9290-1.

[60] Chen J, Yu X, Xu M, Okabe Y, Zhang X, Tuo W. The compressive properties and strengthening mechanism of the middle-trabecular beetle elytron plate. J Sandw Struct Mater 2020;22(4):948–61. https://doi.org/10.1177/1099636218777188.

[61] Du J, Hao P, Liu M, Scarpa F. Multi-cell energy-absorbing structures with hollow columns inspired by the beetle elytra. J Mater Sci 2020;55(10):4279–91. https://doi.org/10.1007/s10853-019-04190-4.

[62] Xiang J, Du J, Li D, Scarpa F. Numerical analysis of the impact resistance in aluminum alloy bi-tubular thin-walled structures designs inspired by beetle elytra. J Mater Sci 2017;52(22):13247–60.

[63] Yu X, Pan L, Chen J, Zhang X, Wei P. Experimental and numerical study on the energy absorption abilities of trabecular–honeycomb biomimetic structures inspired by beetle elytra. J Mater Sci 2019;54(3):2193–204. https://doi.org/10.1007/s10853-018-2958-0.

[64] Chen J, Yu X, Zhang X, Xu Y, Fu Y. The effect of trabecular chamfers on the compressive ductility of beetle elytron plates. Mech Mater 2021;163:104093. https://doi.org/10.1016/j.mechmat.2021.104093.

[65] Chen Q, Pugno N, Zhao K, Li Z. Mechanical properties of a hollow-cylindrical-joint honeycomb. Compos Struct 2014;109(1):68–74. https://doi.org/10.1016/j.compstruct.2013.10.025.

[66] Ajdari A, Jahromi BH, Papadopoulos J, Nayeb-Hashemi H, Vaziri A. Hierarchical honeycombs with tailorable properties. Int J Solids Struct 2012;49(11–12):1413–9. https://doi.org/10.1016/j.ijsolstr.2012.02.029.

[67] Oftadeh R, Haghpanah B, Papadopoulos J, Hamouda AMS, Nayeb-Hashemi H, Vaziri A. Mechanics of anisotropic hierarchical honeycombs. Int J Mech Sci 2014; 81:126–36. https://doi.org/10.1016/j.ijmecsci.2014.02.011.

[68] Mousanezhad D, Haghpanah B, Ghosh R, Hamouda AM, Nayeb-Hashemi H, Vaziri A. Elastic properties of chiral, anti-chiral, and hierarchical honeycombs: a simple energy-based approach. Theor Appl Mech Lett 2016;6(2):81–96. https://doi.org/10.1016/j.taml.2016.02.004.

[69] Di Yu X, Zhang XM, Chen JX, Zhao CQ, Zhao TD, Fu YQ. The flexural property and its synergistic mechanism of multibody molded beetle elytron plates. Sci China Technol Sci 2020;63(5):768–76. https://doi.org/10.1007/s11431-019-1470-5.

[70] Xu M, Pan L, Chen J, Zhang X, Yu X. The flexural properties of end-trabecular beetle elytron plates and their flexural failure mechanism. J Mater Sci 2019;54 (11):8414–25. https://doi.org/10.1007/s10853-019-03488-7.

[71] H. G. Allen, Analysis and design of structural sandwich panels: the commonwealth and international library: structures and solid body mechanics division. Elsevier, 2013.

[72] Burton WS, Noor AK. Assessment of continuum models for sandwich panel honeycomb cores. Comput Methods Appl Mech Eng 1997;145(3):341–60. https://doi.org/10.1016/S0045-7825(96)01196-6.

[73] Hohe J, Becker W. A refined analysis of the effective elasticity tensor for general cellular sandwich cores. Int J Solids Struct 2001;38(21):3689–717. https://doi.org/10.1016/S0020-7683(00)00246-8.

[74] Balawi S, Abot JL. The effect of honeycomb relative density on its effective in-plane elastic moduli: An experimental study. Compos Struct 2008;84(4):293–9. https://doi.org/10.1016/j.compstruct.2007.08.009.

[75] Python, "The Python Language Reference," 2013.

[76] ABAQUS INC, "ABAQUS Analysis User's Manual," 2013.

[77] E. J. Barbero, *Finite element analysis of composite materials using abaqus^TM*. 2013.

[78] Melro AR, Manno R. "Microscale representative volume element: generation and statistical characterization", *Multi-Scale Contin.* Mech Model Fibre-Reinforced Polym Compos 2021:31–54. https://doi.org/10.1016/b978-0-12-818984-9.00002-0.

[79] Chen YJ, Scarpa F, Liu YJ, Leng JS. Elasticity of anti-tetrachiral anisotropic lattices. Int J Solids Struct 2013;50(6):996–1004. https://doi.org/10.1016/j.ijsolstr.2012.12.004.

[80] Burlayenko VN, Sadowski T. Effective elastic properties of foam-filled honeycomb cores of sandwich panels. Compos Struct 2010;92(12):2890–900. https://doi.org/10.1016/j.compstruct.2010.04.015.

[81] Sanami M, Ravirala N, Alderson K, Alderson A. Auxetic Materials for Sports Applications. Procedia Eng 2014;72:453–8. https://doi.org/10.1016/j.proeng.2014.06.079.

[82] Malek S, Gibson L. Effective elastic properties of periodic hexagonal honeycombs. Mech Mater 2015;91(P1):226–40. https://doi.org/10.1016/j.mechmat.2015.07.008.

[83] Gibson LJ, Ashby MF. Celluar_solids_98_Chap4_The mechanics of honeycombs. Cell Solids 2014:93–174. https://doi.org/10.1017/cbo9781139878326.006.

[84] Scarpa F, Panayiotou P, Tomlinson G. Numerical and experimental uniaxial loading on in-plane auxetic honeycombs. J Strain Anal Eng Des 2000;35(5):383–8. https://doi.org/10.1243/0309324001514152.

[85] Harkati E, Daoudi N, Bezazi A, Haddad A, Scarpa F. In-plane elasticity of a multi re-entrant auxetic honeycomb. Compos Struct 2017;180:130–9. https://doi.org/10.1016/j.compstruct.2017.08.014.

[86] Harkati A, Boutagouga D, Harkati E, Bezazi A, Scarpa F, Ouisse M. In-plane elastic constants of a new curved cell walls honeycomb concept. Thin-Walled Struct 2020;149:106613. https://doi.org/10.1016/j.tws.2020.106613.

[87] Harkati EH, Daoudi NEH, Abaidia CE, Bezazi A, Scarpa F. The Elastic uniaxial properties of a center symmetric honeycomb with curved cell walls: effect of density and curvature. Phys Status Solidi Basic Res 2017;254(12):1–10. https://doi.org/10.1002/pssb.201600818.